Journal of Inorganic and Organometallic Polymers and Materials (2021) 31:3481–3495
https://doi.org/10.1007/s10904-021-01959-6

Electromagnetic Interference Shielding Characteristics of $SrTiO_3$ Nanoparticles Induced Polyvinyl Chloride and Polyvinylidene Fluoride Blend Nanocomposites

Jenifer Joseph[1] · Kalim Deshmukh[2] · Arunai Nambi Raj[3] · S. K. Khadheer Pasha[4]

Received: 15 January 2021 / Accepted: 2 March 2021 / Published online: 2 April 2021

Abstract
The current work deals with the synthesis and characterization of strontium titanate ($SrTiO_3$) nanoparticles reinforced polyvinyl chloride (PVC) and polyvinylidene fluoride (PVDF) blend nanocomposite films prepared via a solution casting approach. The structural, thermal, morphological characteristics of the PVC/PVDF/$SrTiO_3$ nanocomposite films were explored through Fourier transform infrared spectroscopy- FTIR, X-ray diffraction–XRD, thermogravimetric analysis–TGA, scanning electron microscopy–SEM and atomic force microscopy–AFM. The electromagnetic interference (EMI) shielding efficiency (SE) of the PVC/PVDF/$SrTiO_3$ nanocomposite films were investigated in Ku-band (12–18 GHz). The EMI shielding result demonstrated the enhancement in EMI SE values with an increase in the $SrTiO_3$ loading. The PVC/PVDF/$SrTiO_3$ nanocomposite exhibits the maximum EMI SE values ~ − 12.51 dB at 10 wt% of $SrTiO_3$ loading. These findings affirm the dominating absorption behaviour of the nanocomposite (73.9%) with an overall shielding ability of 99.6% and negligible transmittance.

Keywords PVC · PVDF · $SrTiO_3$ · Dielectric properties · EMI studies · Ku- band

1 Introduction

Over the years, the composite consisting of dielectric and magnetic materials has been extensively employed in research sectors [1–8]. Such materials are used adversely in various applications including electronic devices, stealth technology and electromagnetic interference (EMI) shielding applications as electromagnetic absorber (EMA) [1, 8]. The need for shielding turns necessity as the harmful electromagnetic radiations (EMR) that arises from the upgrading telecommunication systems tends to pollute the atmosphere. Along with disrupting the function of electronic devices, these dreadful radiations can leave a detrimental impact on the environment and the biological tissues as well, hence blocking EMR is essential [1, 9, 10]. Out of the three predominant shielding mechanisms namely reflection, absorption and multiple reflection, shielding through absorption is preferable as it can attenuate the EMR within the material whereas other techniques can partially harm the environment [11]. Generally, materials with good electric permittivity (ε') and permeability (μ') make an excellent EMR absorber. Moreover, the EMR absorbed on the electric field is estimated by ε', while the EM radiation absorbed in a magnetic field can be measured byμ'. When EM waves strikes the shielding material, the radiation is attenuated and with the dissipation of heat, the energy is lost. The degree of energy loss counts on the values of ε' and μ' and also on the frequency of the wave [1, 12]. Furthermore, materials with improved porosity also play a vital role in increasing the rate of absorption through polarization of EM waves [11].

For the primary reflection-based shielding mechanism, the material requires metals which has certain constraints like a heavyweight, corrosiveness, high cost and difficulty in processing [13]. The absorption technique requires a material with definite electrical conductivity and holds

✉ S. K. Khadheer Pasha
khadheerbasha@gmail.com

[1] Department of Physics, School of Advanced Sciences, VIT University, Vellore, Tamil Nadu 632014, India

[2] New Technologies-Research Center, University of West Bohemia, 30100 Pilsen, Czech Republic

[3] Centre for Biomaterials, Cellular and Molecular Theranostics (CBCMT), VIT University, Vellore, Tamil Nadu 632014, India

[4] Department of Physics, VIT-AP University, Amaravati, Guntur, Andhra Pradesh 522501, India

electric–magnetic dipoles. Hence, materials with superior magnetic permeability and dielectric constant are preferable [13, 14]. Though high k-materials offer various advantages for absorption-based EMI shielding, it also opens up some key constraints such as weakening the mechanical properties, narrowed band actions and processing difficulties [15]. Hence, polymer-based composites were developed to resolve those drawbacks and to achieve an efficient EMI shielding material [16]. Polymer nanocomposites (PNCs) can be made by reinforcing nanofillers within the polymer matrix. The integration of nanofiller into polymer matrix formulates a synergistic effect on the properties of PNCs. These revolutionary effects of PNCs make them applicable in various sectors including energy storage devices, sensors, EMI shielding, biomedical engineering and even as a replacement for metal alloys in automobile industries [11, 17–24]. Although PNCs have various applications and different sorts of polymer composites have been built up, the ultimate objective of current work is to achieve a light weight and economical EM radiation blocking material. Several works have been reported where conductive nano-fillers having high aspect ratio for instance single-walled carbon nanotubes (SWCNTs) [25], multi-walled carbon nanotubes (MWCNTs) [26] and metal nanowires [27] were studied extensively in this context due to their impressive properties coupled with their unique microstructure [14]. For instance, Fayzan Shakir et al. [28] have studied the EMI SE of PVC/PANI/GNP composites which showed EMI SE of ~ 51 dB in the Ku band. Kim et al. [29] reported that MWCNT/PVDF/PVP composite exhibits EMI SE of 18–21 dB in the frequency range of 10 to 1500 MHz. The foam composites comprising functionalized graphene and PVDF show ~ 20 dB in X-band [30]. Muzaffar et al. [31] reported PVC/$BaTiO_3$/NiO nanocomposites with a maximum EMI SE of − 18.7 dB in the Ku band. Moreover, several reports have been published on various carbon-based filler reinforced PNCs for EMI shielding applications [32, 33]. Though all these material facilitates effective EMR shielding behavior, on the other hand, their fabrication process was highly complex, tedious and also expensive [34, 35]. Thus, the material has to be chosen in such a way that it should produce good EMI SE and also should be budget-friendly.

Polyvinylidene fluoride (PVDF) is a flexible, piezoelectric material with low density that can form great conductive PNCs for shielding applications [13]. Also, PVDF offers a very high breakdown strength [36], high weather and chemical resistance and high dielectric constant. The conductivity in PVDF can be induced when the conductive filler is uniformly distributed into the polymer matrix [37]. On the other hand, PVC is one of the most promising polymer matrices being versatile, lightweight and flexible it increases the workability of the composites [38]. It has the potential to withstand atmospheric conditions like extreme heat and radiation which is essential in practical applications. Thus, PVC can be a potential candidate in shielding applications [11]. The motivation behind choosing strontium titanate ($SrTiO_3$) nanoparticles as nanofiller is that the incorporation of conducting ceramic ferroelectric oxides into the polymer matrix can offer a good energy device with a high dielectric constant along with appreciable energy storage density [39]. Also, under the electric field, the ferroelectric material performs a rapid dipole moment and their orientation switches (coercive field) which can attenuate the harmful radiations through absorption [40]. These peculiar properties of ferroelectric perovskite oxides can also be implemented in high-k- materials, energy storage devices, electromechanical transducers etc. [41]. So far as we know, no report was published on PVC/PVDF/$SrTiO_3$ nanocomposites which are investigated here as a potential shield for blocking EM radiation.

2 Experimental

2.1 Materials

PVDF was supplied by Pragathi plastics Pvt. Ltd., India. PVC of average molecular weight 43,000 g/mol and $SrTiO_3$ nanoparticles with an average particle size of 50 nm are purchased from Sigma-Aldrich, India. N, N dimethylformamide (DMF) was purchased from the Sisco Research Laboratory—SRL, Pvt. Ltd., from India.

2.2 Synthesis Process of PVC/PVDF/$SrTiO_3$ Nanocomposite Films

The PVC/PVDF/$SrTiO_3$ nanocomposite films have been synthesized at different loading (0 to 10 wt%) of $SrTiO_3$ nanoparticles via the solution blending technique. Initially, the PVC was dissolved in DMF at 60 °C for 1 h. Simultaneously, PVDF was dissolved in the same solvent at 60 °C for 4 h. On the other hand, $SrTiO_3$ nanoparticles were dispersed separately in DMF in an ultrasonicating bath for 1 h. To this dispersed $SrTiO_3$ nanoparticles, PVC/PVDF blend solution was added. The PVC/PVDF/$SrTiO_3$ dispersion was then stirred overnight on a magnetic stirrer to get a homogeneous mixture followed by its casting onto a Teflon petri dish and drying at 60 °C for 6 h in a hot air oven. The dried samples were peeled away from the petri dish and utilized for various analyses. The synthesis protocol and the feed compositions are shown in Fig. 1 and Table 1.

2.3 Characterizations

The PVC/PVDF/$SrTiO_3$ nanocomposite films were characterized using Fourier transform

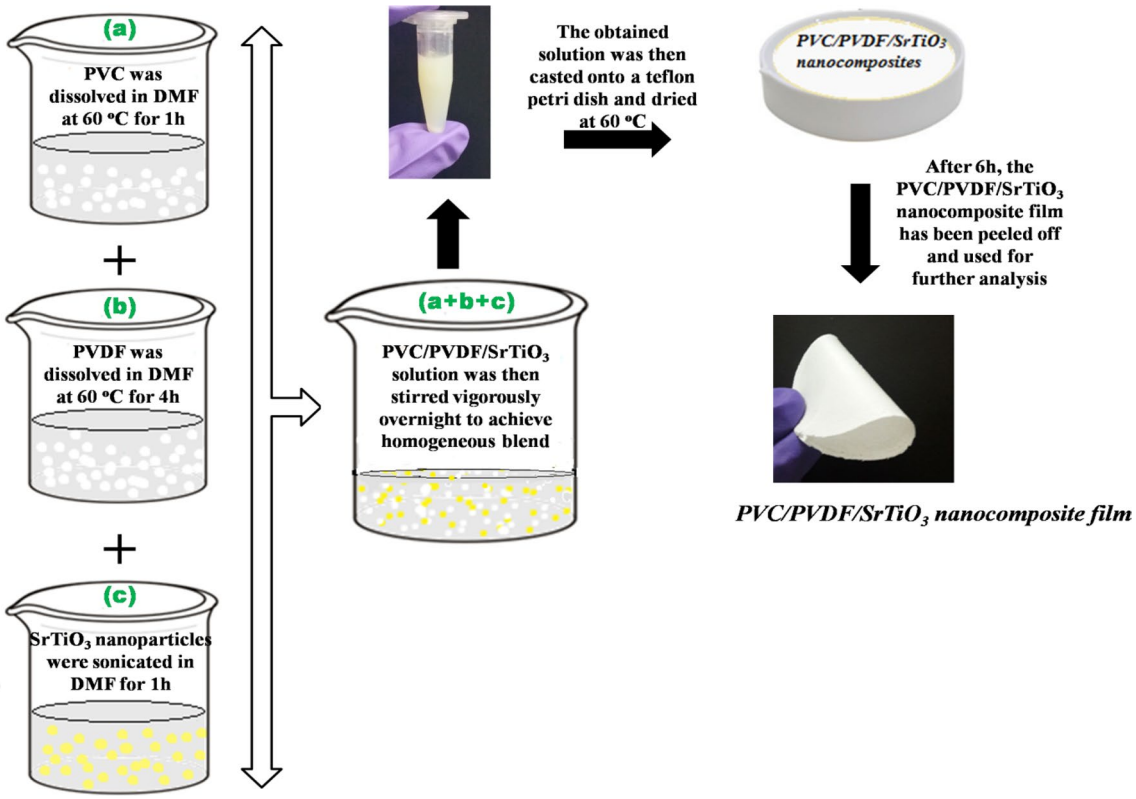

Fig. 1 Protocol of the synthesis of PVC/PVDF/$SrTiO_3$ nanocomposite films

Table 1 Feed compositions of PVC/PVDF/$SrTiO_3$ nanocomposite films

Sample code	PVC (wt%)	PVDF (wt%)	$SrTiO_3$ (wt%)
a	100	0	0
b	0	100	0
c	40	60	0
d	40	58	2
e	40	56	4
f	40	54	6
g	40	52	8
h	40	50	10

infrared Spectrophotometer between the wave number 400–4000 cm^{-1} (Shimadzu, IRAffinity -1, Japan),

XRD study of PVC/PVDF/$SrTiO_3$ nanocomposite films was analysed using Bruker AXS D8 focus advanced X-ray diffraction meter (Rigaku, Tokyo, Japan). The samples were scanned in the 2θ range between 10 and 90° through Cu-K α radiation of wavelength, λ = 1.54 Å with the scanning speed 1°/min and step size of 0.01° respectively.

The thermal durability of PVC/PVDF/$SrTiO_3$ nanocomposite films was analysed using thermogravimetric analyser (TGA) SDTQ600 TA equipment in the temperature range between 25 and 700 °C with a heating rate of 10 °C/min.

The surface topography of the PVC/PVDF/$SrTiO_3$ nanocomposite films was obtained using the atomic force microscope (AFM) Nano Surf Easy Scan2 from Switzerland. The measurements were done in tapping mode.

Hitachi Quanta 200 scanning electron microscope was employed to analyze the surface morphology of the PVC/PVDF/$SrTiO_3$ nanocomposite films. The SEM images of the samples were acquired using an accelerating voltage of 15 kV.

The dielectric properties of the samples were evaluated in the temperature range 40–150 °C and in the frequency range between 1 Hz and 20 MHz through Wayne Kerr 6500B Precision Impedance Analyzer, Chichester, West Sussex, UK.

The PVC/PVDF/$SrTiO_3$ nanocomposite films have been scrutinized for their EMI shielding properties. Specimens with 3 × 3 cm dimension were positioned on a sample holder that was linked to a Hewlett Packard 8510C Vector Network Analyzer (VNA), USA. The EMR in the broad range of frequency between 12 and 18 GHz (Ku band) were encountered with the sample and scattering parameters respective to transmission (S12/S21) and reflection (S11/S22) of the incident EMR was estimated [2].

3 Result and Discussions

3.1 FTIR Spectroscopy Studies

FTIR studies are done to confirm the existence of corresponding functional groups of material. Figure 2a–i displays the FTIR spectra of PVC/PVDF/$SrTiO_3$ nanocomposite films. Figure 2a depicts the FTIR spectrum of $SrTiO_3$ nanoparticles where the absorption bands around 480 and 542 cm^{-1} are assigned to TiO_6 octahedron bending and stretching vibration respectively [42]. The absorption peak around 1459 cm^{-1} attributed to the bending vibration of H–O–H from the adsorbed H_2O [42]. Figure 2b shows the FTIR spectrum of pristine PVC. The band at 955 cm^{-1} corresponds to the rocking vibration of CH_2 and the band at 1324 cm^{-1} is due to the $–CH_2$ deformation while the band at 1428 cm^{-1} represents the wagging of methylene groups in PVC [43]. The FTIR spectrum of pristine PVDF is shown in Fig. 2c. The peak at 840 cm^{-1} ascertains the presence of β phase stretching vibration [44]. The band around 1152 cm^{-1} corresponds to the symmetrical stretching of $–CF_2$ and the band at 1398 cm^{-1} attributes to the scissoring or in-plane bending of CH_2 groups of PVDF [44]. Figure 2d–i represents the FTIR spectra of PVC/PVDF/$SrTiO_3$ nanocomposites where the existence of FTIR peaks of an individual component affirms the functional groups present in the corresponding component. Moreover, it is observed that the PVC/PVDF blend matrix shows no significant shift in the peaks with the addition of nanofiller.

3.2 X-Ray Diffraction Studies

The XRD pattern of $SrTiO_3$ nanoparticles can be seen in Fig. 3a. The good crystallinity of $SrTiO_3$ nanoparticles is confirmed by the presence of prominent XRD peaks correspond to 100, 110, 111, 200, 211, 220, 310, 311 and 222 planes with peak positions at $2\theta = 22.9°$, 32.5°, 40°, 46.6°, 57.9°, 68°, 77.3°, 81.9° and 86.4° respectively [45]. From the XRD pattern, the particle size of the $SrTiO_3$ crystallites was determined to be 25.48 nm using Eq. (1),

$$D = \frac{K\lambda}{\beta cos\theta} \tag{1}$$

From JCPDS card no: 35-0734, it was confirmed that the characteristic XRD peaks of $SrTiO_3$ nanoparticles belong to the cubic perovskite structure with space group Pm3m [45]. Figure 3b, reveals the amorphous nature of PVC with those two broad peaks at $2\theta = 29.2$ and $2\theta = 40.1°$ respectively [46]. The XRD pattern of pristine PVDF is illustrated in Fig. 3c, which shows three characteristic XRD peaks of PVDF at $2\theta = 19.1$, 34.4, and 40.2° respectively, where, the broad peak at $2\theta = 19.1°$ indicates the α-phase of PVDF [19]. Figure 3d–i, depicts the XRD patterns of PVC/PVDF blend and the PVC/PVDF/$SrTiO_3$ nanocomposites with different wt% of $SrTiO_3$ nanoparticles. The result shows the presence of the characteristic peaks of both polymers and $SrTiO_3$ nanoparticles.

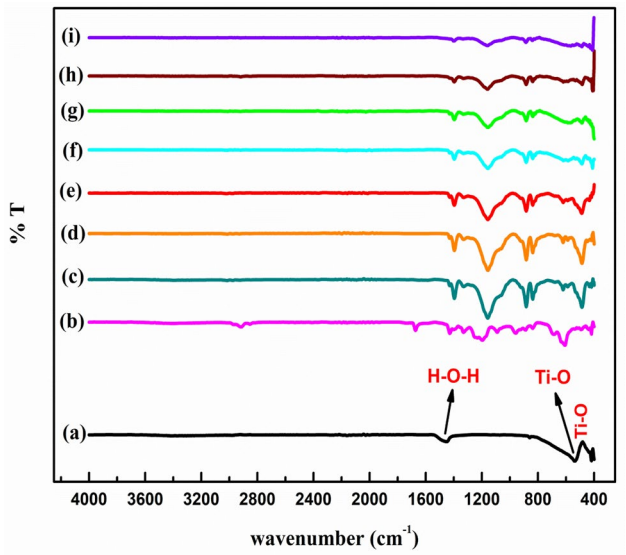

Fig. 2 FTIR spectra of PVC/PVDF/$SrTiO_3$ nanocomposite films. (a) $SrTiO_3$, (b) pristine PVC, (c) pristine PVDF, (d) PVC/PVDF, (e) 2 wt% $SrTiO_3$, (f) 4 wt% $SrTiO_3$, (g) 6 wt% $SrTiO_3$, (h) 8 wt% $SrTiO_3$, (i) 10 wt% $SrTiO_3$

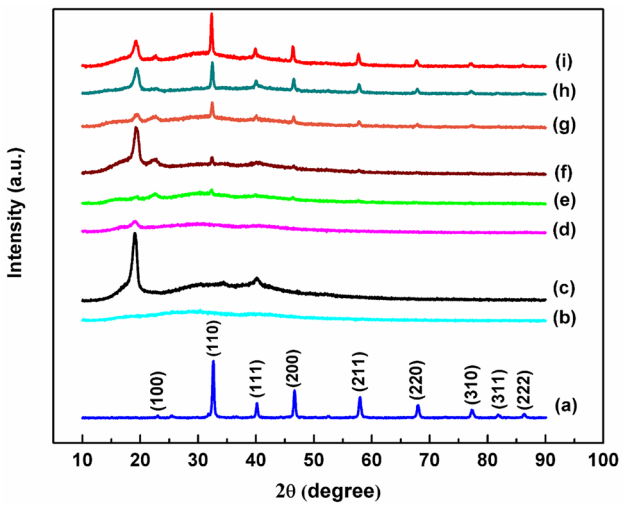

Fig. 3 XRD patterns of PVC/PVDF/$SrTiO_3$ nanocomposite films. (a) $SrTiO_3$, (b) pristine PVC, (c) pristine PVDF, (d) PVC/PVDF, (e) 2 wt% $SrTiO_3$, (f) 4 wt% $SrTiO_3$, (g) 6 wt% $SrTiO_3$, (h) 8 wt% $SrTiO_3$, (i) 10 wt% $SrTiO_3$

3.3 Thermogarvimetric Analysis

Figure 4 depicts the TGA thermograms of $SrTiO_3$ nanoparticles, PVDF, PVC and PVC/PVDF/$SrTiO_3$ nanocomposites. From Fig. 4a it was observed that the $SrTiO_3$ nanoparticles are thermally stable with an overall weight loss of about 2.25% in the entire temperature range. Figure 4b depicts the thermogram of pristine PVC film. The weight loss between ambient temperatures and 160 °C corresponds to the dispersion of volatile components and the trapped solvent [11]. The sample remains thermally stable in the temperature range between 161 and 224 °C. The thermogram revealed that PVC has undergone two strong decomposition stages; one is in the temperature range between 225 and 350 °C due to the decomposition of PVC with the release of HCL where the sample experiences a drastic weight loss of 57.6% [47].

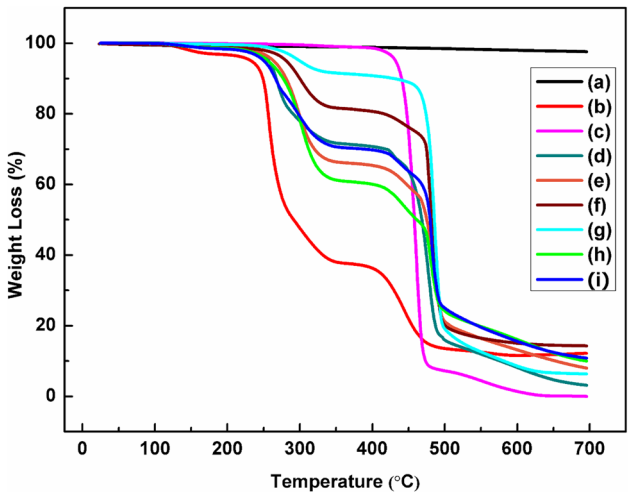

Fig. 4 TGA thermograms of PVC/PVDF/$SrTiO_3$ nanocomposite films. (a) $SrTiO_3$, (b) pristine PVC, (c) pristine PVDF, (d) PVC/PVDF, (e) 2 wt% $SrTiO_3$, (f) 4 wt% $SrTiO_3$, (g) 6 wt% $SrTiO_3$, (h) 8 wt% $SrTiO_3$, (i) 10 wt% $SrTiO_3$

The latter weight loss between 401 and 500 °C is comparatively shorter than the previous decomposition; in this stage, the sample has a weight loss of 22.4% which can be attributed to the disintegration of the polyene backbone of PVC that creates volatile aromatic compounds and a substantial carbonaceous residue [11, 47]. The TGA curve of PVDF was displayed in Fig. 4c, which demonstrates that PVDF film is quite stable until 410 °C where the loss of HF takes place that leads to the formation of polyaromatization followed by carbonization and at 700 °C the residue of 2.16% is left [44]. Figure 4d shows the TGA curve of PVC/PVDF blend films which showed good stability until 224 °C. The TGA thermogram displayed two strong degradation stages, the initial decomposition between 225 and 350 °C can be assigned to the loss of HCl in PVC [47]. Whereas the sample remains stable in the temperature range between 351 and 409 °C, the second stage weight loss between 410 and 497 °C is due to the loss of PVDF backbones at this temperature range [48]. Thus it can be interpreted that PVDF is thermally more stable than that of PVC. The TGA thermogram of PVC/PVDF blend film reveals that the inclusion of PVDF has enhanced the thermal stability of PVC. Figure 4e–i shows the TGA thermogram of PVC/PVDF/$SrTiO_3$ nanocomposite films which reveals the thermal stability of the nanocomposite film. Also, the thermal stability of PVDF is better than the PVC/PVDF blend films. This indicates that the addition of PVC to PVDF reduces the thermal stability of nanocomposite film. The $SrTiO_3$ nanoparticles show great thermal stability, hence the mechanism of thermal decomposition and carbonization of the PVC and PVDF are shown in Fig. 5 [49].

3.4 Morphological Studies

AFM study has been carried out in tapping mode to understand the surface topography and roughness of the PNCs. Figure 6a–f depicts the 2D topographic images of PVC/

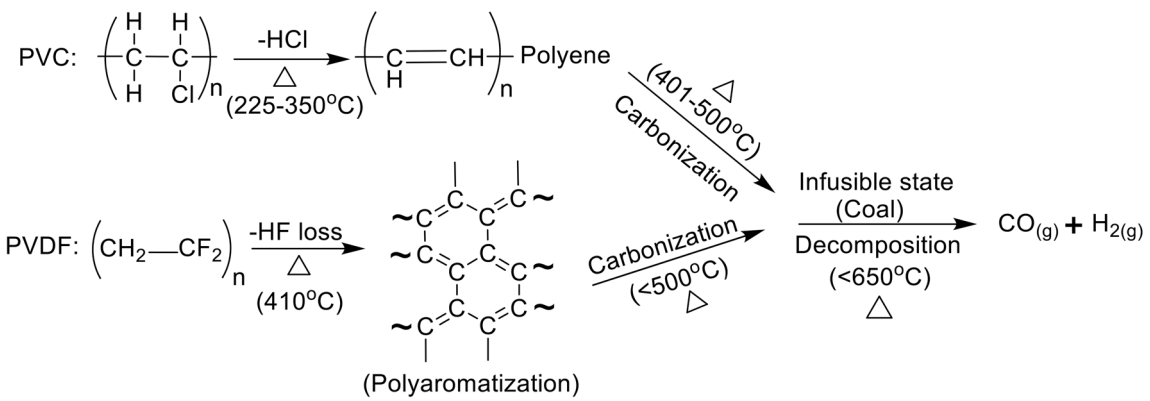

Fig. 5 Mechanism of thermal decomposition and carbonization of PVC and PVDF

PVDF/$SrTiO_3$ nanocomposite films. The surface roughness values (Sa–Sq) in nm at different $SrTiO_3$ loading are revealed in Table 2. From the outcome, it can be observed that the surface roughness of PVC (Fig. 6a) is more than that of PVDF (Fig. 6b). The roughness values increased when the polymers are blended together as can be seen in (Fig. 6c). Figure 6d–f depicts the AFM topographic images of the nanocomposite at different loadings of $SrTiO_3$ nanoparticles.

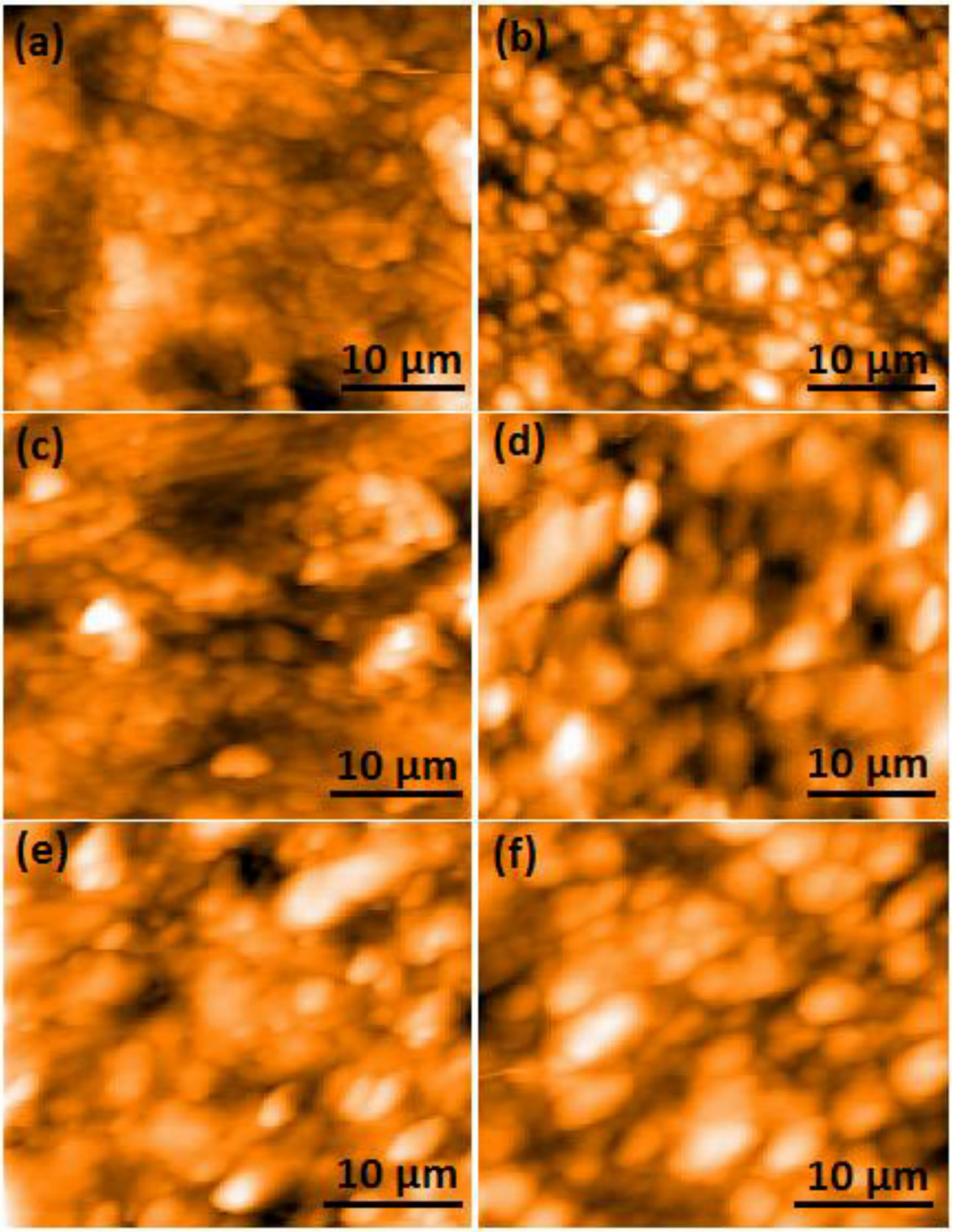

Fig. 6 AFM topographic images of PVC/PVDF/$SrTiO_3$ nanocomposite films. **a** pristine PVC, **b** pristine PVDF, **c** PVC/PVDF, **d** 2 wt% $SrTiO_3$, **e** 6 wt% $SrTiO_3$, **f** 10 wt% $SrTiO_3$

Table 2 Surface roughness parameters of PVC/PVDF/$SrTiO_3$ nanocomposite films at different $SrTiO_3$ loading

PVC/PVDF/$SrTiO_3$ compositions (wt%)	Surface roughness (Sa–Sq) nm
100/0/0	15
0/100/0	12
40/60/0	19
40/58/2	38
40/56/4	25
40/54/6	40
40/52/8	29
40/50/10	49

At the maximum loading of the nanoparticles, the nanocomposite exhibits maximum roughness attributing to the fine dispersion and better interfacial interaction of the nanofiller with the PVC/PVDF blend [50]. The microstructures of the PNCs were further studied using SEM analysis. Figure 7 shows the SEM images of PVC/PVDF/$SrTiO_3$ nanocomposites. From the overview of the images, it is evident that the pristine PVC (Fig. 7a) and PVDF films (Fig. 7b) have comparatively smoother surfaces than their blend (Fig. 7c). The SEM micrograph of PVC/PVDF blend film depicted in Fig. 7c illustrates the surface of the sample with the formation of small and large pores. This porosity can be associated with the highly tangled polymeric chains formed during the blending of these polymers [51]. Figure 7d–f displays the SEM micrograph of PNCs with different loadings of $SrTiO_3$ nanoparticles. In addition to the presence of porosity that developed from the polymer blend matrix, it is observed that the agglomeration improves when nanofiller loading increases which signify the superior interfacial interaction between the filler and the polymer matrices [52].

3.5 Dielectric Properties

Figure 8a depicts the dielectric constant of pristine PVC. The result shows that PVC has a maximum dielectric constant (ε) of 1.2 at a lower frequency (1 Hz, 150 °C). The temperature dependence of dielectric properties of pristine PVDF can be seen in Fig. 8b where ε of about 134 (1 Hz, 150 °C) was observed [53]. The dielectric response of the PVC/PVDF polymer blend was shown in Fig. 8c compared to the pristine PVDF, the ε of the PVC/PVDF polymer blend is decreased to $\varepsilon = 65$ (1 Hz, 150 °C) which may be due to the influence of PVC. The ε of PVC/PVDF/$SrTiO_3$ nanocomposite films at various $SrTiO_3$ nanofiller loading (2 to 10 wt %) can be observed from Fig. 8d–h. The result confirms that the overall ε of the PNCs increases as the composition of $SrTiO_3$ nanoparticle increases. It can be observed that, as the degree of agglomeration increases, the dielectric constant of the composites is also enhanced. This enhancement in dielectric constant can be attributed to the number of regions of the enriched electric field by the side of the applied field amidst the particles in agglomerate [54]. Thus, the sudden drop in the ε of the composites with 4 and 8 wt% of $SrTiO_3$ loading can be interpreted to its lesser agglomeration (roughness) [54]. It can be noted that for all the samples the dielectric constant decreases gradually at higher frequencies whereas it falls abruptly at lower frequencies [54]. The scattering of charge and the molecule chaotic thermal oscillation causes this rapid drop in dielectric constant with respect to the frequency. Every sample exhibits maximum dielectric constant at higher temperatures due to the phenomenon called space charge polarization [54]. At lower temperatures the dipoles are not aligned appropriately and the orientation of the dipoles will be facilitated at elevated temperatures [54]. Therefore, increased polarization gives rise to increased dielectric constant. The PVC/PVDF/$SrTiO_3$ nanocomposite films exhibit maximum ε of 163 (1 Hz, 150 °C) at 10 wt% of $SrTiO_3$ loading. Figure 9a depicts the dielectric loss of pristine PVC, from the result it can be noted that the maximum tan δ of 45 is attained at higher temperature (1 Hz, 150 °C). Figure 9b shows the tan δ plot of pristine PVDF, where the maximum tan δ of 7.82 is obtained at higher temperature (50 Hz, 150 °C). Figure 9c the dielectric loss of the polymer blend is comparatively lesser ($\tan\delta = 4.5$, 10 Hz, 150 °C) than that of pristine PVC and PVDF films, which may be due to the higher ratio of PVDF in the composite than PVC. Figure 9d–h shows the dielectric loss of PVC/PVDF/$SrTiO_3$ nanocomposites at various wt% of $SrTiO_3$ loading. The minimum dielectric loss was observed to be 2.1 at 10 wt% (Fig. 9h) of the nanofiller which is comparatively lesser than other composites. Thus among all ratios, 10 wt% of the $SrTiO_3$ loading provides the highest dielectric constant with the lowest dielectric loss which is an essential characteristic for an ideal energy storage device.

3.6 EMI Shielding Properties

EMI shielding is the process of attenuating the EMR that interacts with the sample and acts as a shield. The EMI SE of a material can be calculated from Eq. (2).

$$\text{EMI SE} = 10\log\left(P_I/P_T\right) = 10\log\left(1/T\right)dB \tag{2}$$

where P_T and P_I represent the power of transmitted and incident radiations [11]. Figure 10 reveals the EMI SE of PVC/PVDF/$SrTiO_3$ nanocomposites in the broadband frequency ranging from 12 to 18 GHz (Ku-band). The obtained EMI SE values were summarized in Table 3. The poor SE of PVC in Fig. 10a is witnessed with SE value around − 1 dB. Hence, PVC is absolutely transparent to EM waves in the analyzed frequency range [11]. From Fig. 10b it can be

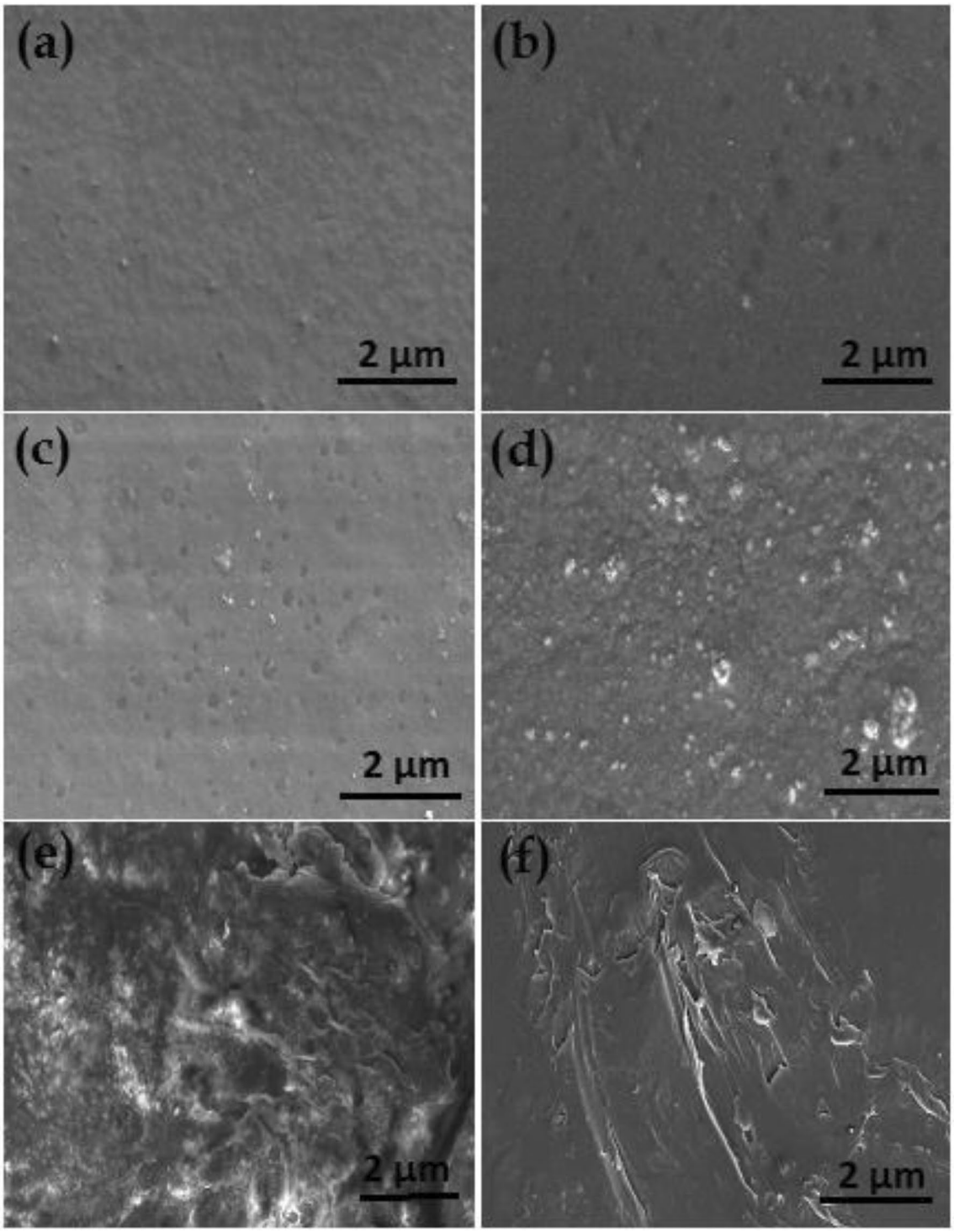

Fig. 7 SEM micrographs of PVC/PVDF/$SrTiO_3$ nanocomposite films. **a** pristine PVC, **b** pristine PVDF, **c** PVC/PVDF blend, **d** 2 wt% $SrTiO_3$, **e** 6 wt% $SrTiO_3$, **f** 10 wt% $SrTiO_3$

noticed that the shielding behavior of pristine PVDF is comparatively better (− 4.2 dB) than that of PVC film. The shielding performance of the PVC/PVDF blend in Fig. 10c affirms better EMI SE than that of individual polymers. Figure 10d–i depicts the EMI SE spectra of PVC/PVDF/$SrTiO_3$ nanocomposites with different wt% of $SrTiO_3$ nanoparticles. The SE of − 6.55, − 7.61, − 10.26, − 11.77 and − 12.51 dB was obtained for 2, 4, 6, 8 and 10 wt% of $SrTiO_3$

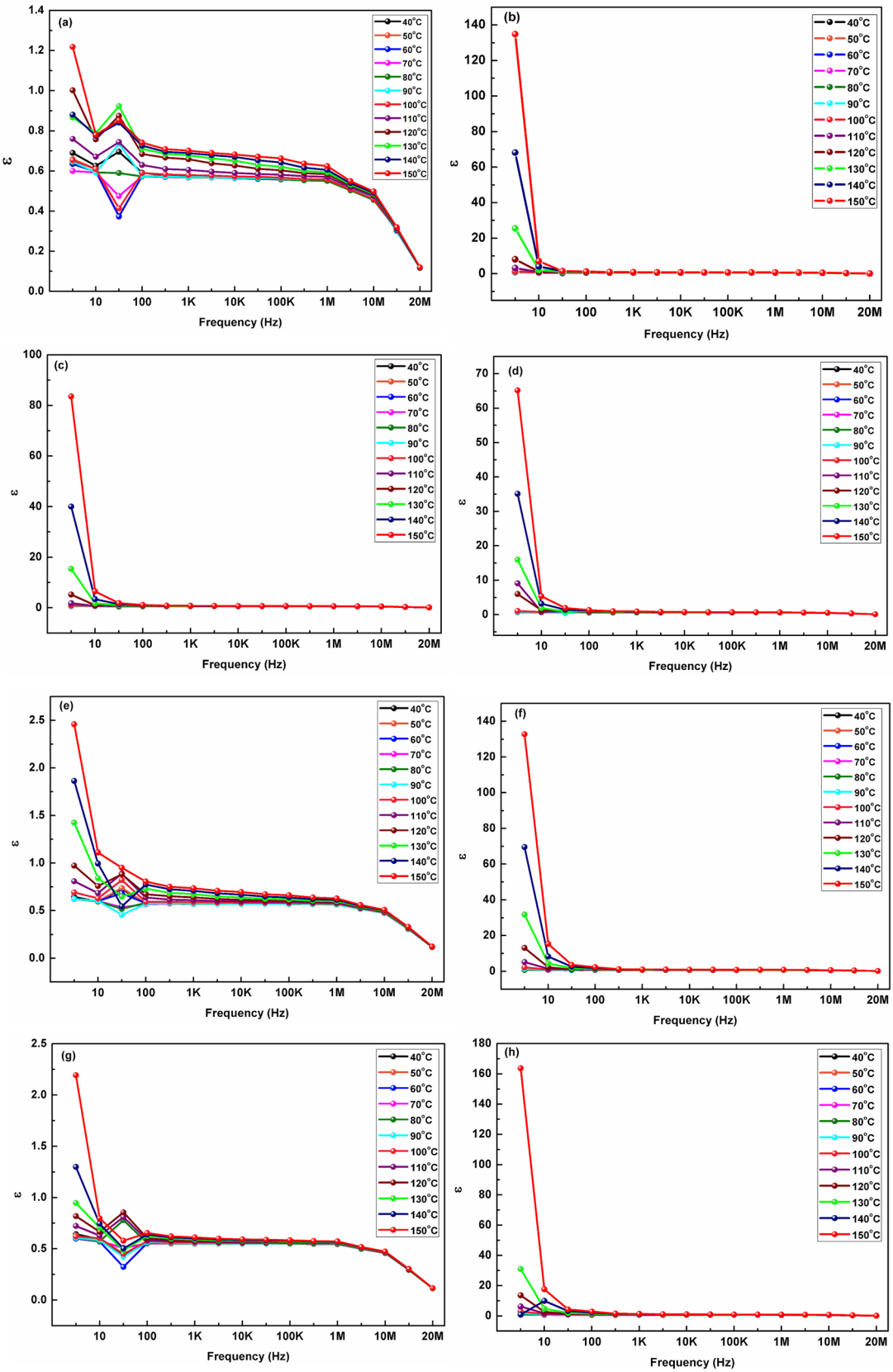

Fig. 8 Dielectric constant graphs of **a** pristine PVC film, **b** pristine PVDF film, **c** PVC/PVDF blend film, **d** PVC/PVDF/$SrTiO_3$ nanocomposite films with 2 wt%, **e** 4 wt%, **f** 6 wt%, **g** 8 wt%, and **h** 10 wt% $SrTiO_3$ content

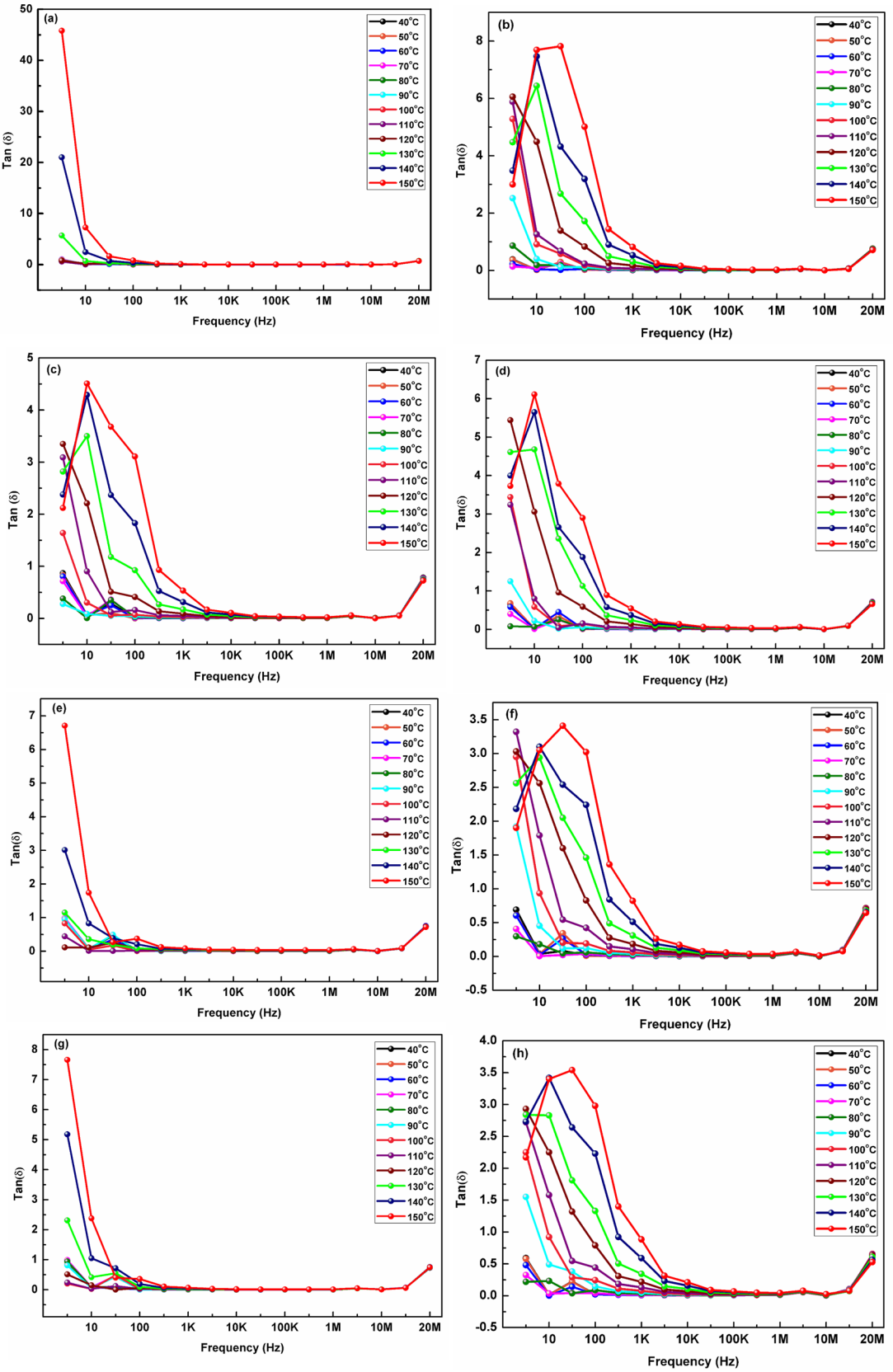

Fig. 9 Dielectric loss graphs of **a** pristine PVC film, **b** pristine PVDF film, **c** PVC/PVDF blend films, **d** PVC/PVDF/$SrTiO_3$ nanocomposite films with 2 wt%, **e** 4 wt%, **f** 6 wt%, **g** 8 wt%, and **h** 10 wt% $SrTiO_3$ content

Table 3 EMI SE of PVC/PVDF/$SrTiO_3$ nanocomposite films in Ku band

Frequency in (GHz)	SE in dB							
	PVC	PVDF	PVC/PVDF	$SrTiO_3$ loading at different wt%				
				2	4	6	8	10
12	− 1.04	− 4.24	− 5.36	− 6.55	− 7.61	− 10.26	− 11.77	− 12.51
13	− 1.03	− 4.22	− 5.33	− 6.54	− 7.57	− 10.24	− 11.72	− 12.49
14	− 1.03	− 4.19	− 5.32	− 6.53	− 7.55	− 10.21	− 11.70	− 12.48
15	− 1.02	− 4.14	− 5.29	− 6.52	− 7.54	− 10.20	− 11.69	− 12.47
16	− 1.00	− 4.11	− 5.26	− 6.50	− 7.53	− 10.19	− 11.67	− 12.47
17	− 1.00	− 4.08	5.26	− 6.49	− 7.52	− 10.18	− 11.65	− 12.45
18	− 1.00	− 4.02	− 5.25	− 6.47	− 7.46	− 10.17	− 11.65	− 12.44

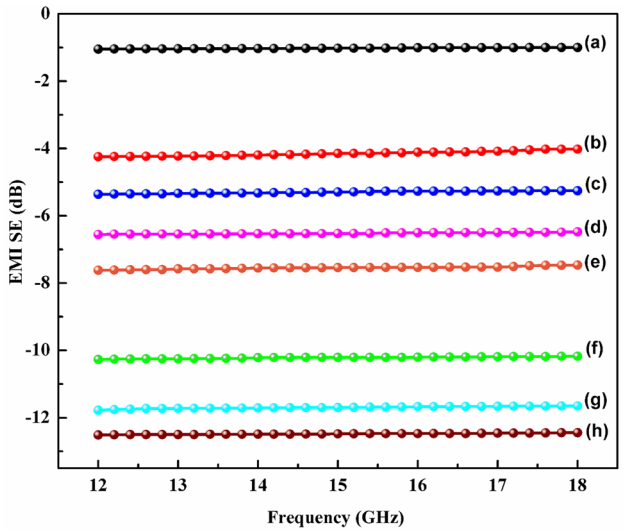

Fig. 10 EMI shielding properties of PVC/PVDF/$SrTiO_3$ nanocomposite films in Ku band (a) pristine PVC, (b) pristine PVDF, (c) PVC/PVDF, (d) 2 wt% $SrTiO_3$, (e) 4 wt% $SrTiO_3$, (f) 6 wt% $SrTiO_3$, (g) 8 wt% $SrTiO_3$, (h) 10 wt% $SrTiO_3$

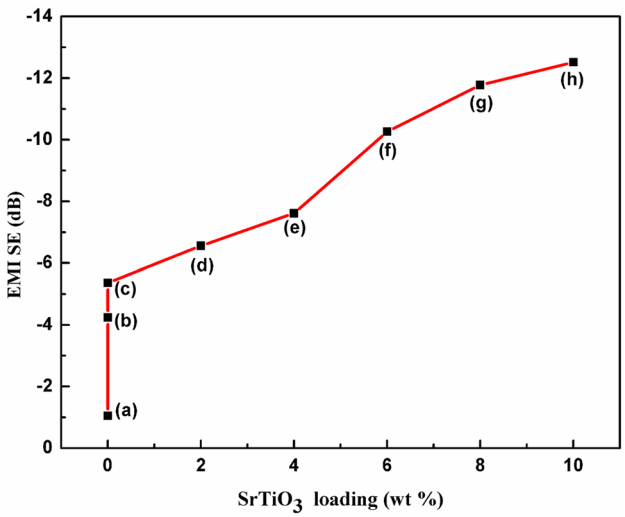

Fig. 11 EMI SE Versus $SrTiO_3$ loading trend of PVC/PVDF/$SrTiO_3$ nanocomposite films in Ku band (a) pristine PVC, (b) pristine PVDF, (c) PVC/PVDF, (d) 2 wt% $SrTiO_3$, (e) 4 wt% $SrTiO_3$, (f) 6 wt% $SrTiO_3$, (g) 8 wt% $SrTiO_3$, (h) 10 wt% $SrTiO_3$

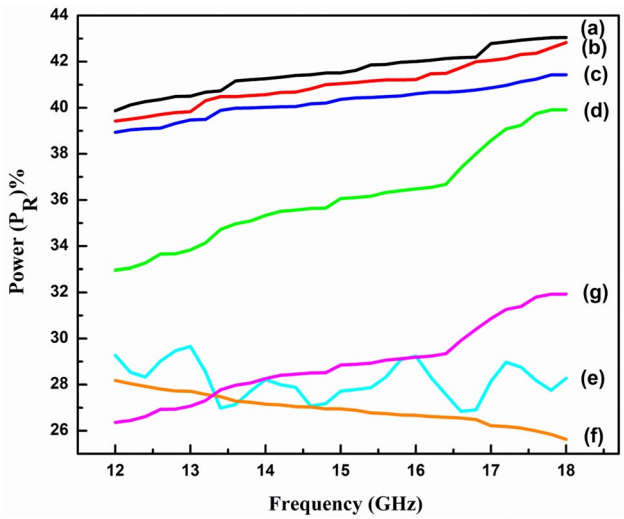

Fig. 12 Reflection power (%) of PVC/PVDF/$SrTiO_3$ nanocomposite films in Ku band (a) pristine PVDF, (b) PVC/PVDF, (c) 2 wt% $SrTiO_3$, (d) 4 wt% $SrTiO_3$, (e) 6 wt% $SrTiO_3$, (f) 8 wt% $SrTiO_3$, (g) 10 wt% $SrTiO_3$

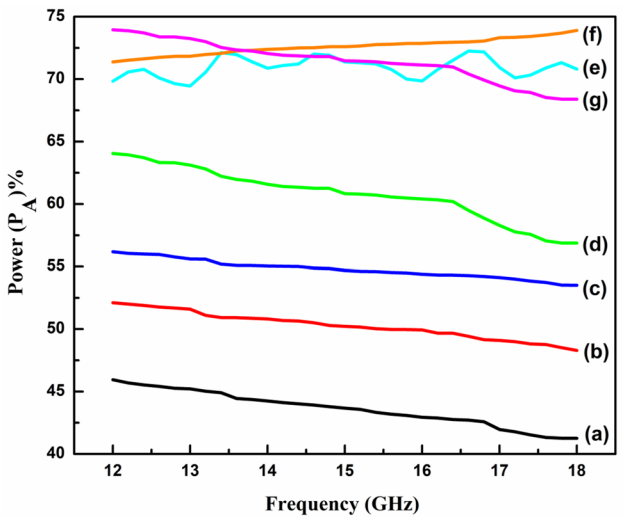

Fig. 13 Absorption power (%) of PVC/PVDF/$SrTiO_3$ nanocomposite films in Ku band (a) pristine PVDF, (b) PVC/PVDF, (c) 2 wt% $SrTiO_3$, (d) 4 wt% $SrTiO_3$, (e) 6 wt% $SrTiO_3$, (f) 8 wt% $SrTiO_3$, (g) 10 wt% $SrTiO_3$

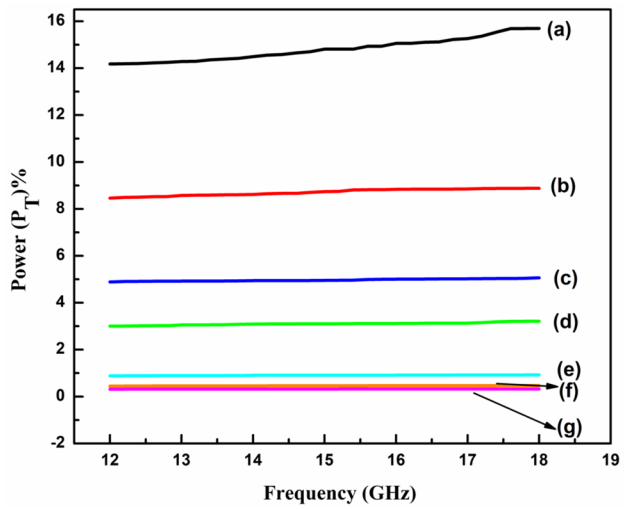

Fig. 14 Transmission power (%) of PVC/PVDF/$SrTiO_3$ nanocomposite films in Ku band (a) pristine PVDF, (b) PVC/PVDF, (c) 2 wt% $SrTiO_3$, (d) 4 wt% $SrTiO_3$, (e) 6 wt% $SrTiO_3$, (f) 8 wt% $SrTiO_3$, (g) 10 wt% $SrTiO_3$

content respectively. From Fig. 11a–h it can be ascertained that $SrTiO_3$ enriches the overall shielding performance of the nanocomposites and maximum EMI SE (− 12.51) was achieved at maximum loading (10 wt%) of $SrTiO_3$.

3.7 EMI Shielding Mechanism of PVC/PVDF/$SrTiO_3$ Nanocomposite Films

The incident EMR striking on a radiation blocking material can be segregated as reflected power, absorbed power and transmitted power. The coefficients of respective reflectance (R), absorbance (A) and transmittance (T) power are expressed as

$$R + A + T = 1 \tag{3}$$

The overall EMI SE (SE_{Total}) may be obtained by the summation of the three predominant shielding techniques such as reflection (SE_R), absorption (SE_A), multiple reflections (SE_M) which are mathematically expressed as,

$$\text{EMI SE}_{Total}(dB) = SE_R + SE_A + SE_M \tag{4}$$

SE_M can be ignored in cases where $SE_{Total} \geq 10$ dB, thus Eq. (4) can be re-written as,

$$\text{EMI SE}_{Total}(dB) = SE_R + SE_A \tag{5}$$

It is necessary to unfold the segregated shielding mechanism of the nanocomposite material. Figures 12, 13 and 14 shows the power (P_R, P_A and P_T) in % versus frequency plots where the % of reflection, absorption and transmission of EM radiation by the shielding material is depicted. Since PVC has poor potential to shield EM radiation, the sample was not analysed to find its dominating shielding mechanism. As the maximum loading of $SrTiO_3$ offers the best shielding results (Fig. 11h) its P_R, P_A and P_T are discussed here. Figure 12 shows the reflectance power versus frequency trend. It can be noted that the reflectance behaviour of the sample decreased with an increase in nanofiller loading. Also, it is observed that the % of reflectance increases gradually as the frequency range increases. The total reflectance varies between 26.4 and 31.9% (12–18 GHz, 10 wt% of $SrTiO_3$). Figure 13 illustrates the absorbance power versus frequency graphs. At 10 wt% of $SrTiO_3$ loading (Fig. 13g) the specimen exhibits outstanding absorption behaviour of EM radiation. PA % enhances with an increase in the loading of the nanoparticles and at high loading, the absorption values range from 73.9 to 68.4% (12–18 GHz) therefore, this nanocomposite can be an excellent EM absorber. The absorption performance of the sample can be understood when it is correlated with the reflection loss (RL) of the shielding material which can be mathematically expressed as [55, 56],

$$RL = 20log\left|\frac{Z_{in} - 1}{Z_{in} + 1}\right| \tag{6}$$

$$Z_{in} = \sqrt{\mu_r/\varepsilon_r}\tan h\left[j(2\pi fd/C)\sqrt{\varepsilon_r\mu_r}\right] \tag{7}$$

Z_{in}: Input impedance, C: Velocity of EM waves (in free space), f: Corresponding frequency, d: Thickness of the shielding material.

It is known that an EM absorber should have high permittivity and permeability thereby it can attenuate the radiation through electric and/or magnetic dipoles [57]. Thus, Fig. 13g shows the highest absorption of 73.9% with the highest relative permittivity, $\varepsilon' = 163$. The P_T in % versus frequency plot shown in Fig. 14 affirms the very minimal transmittance of the sample. This makes the PVC/PVDF/$SrTiO_3$ nanocomposite films an ideal EMI shielding material. At 10 wt % of $SrTiO_3$ loading Fig. 14g the composite exhibits a negligible transmittance which ranges between 0.31 and 0.32% (12–18 GHz).

4 Conclusions

The PVC/PVDF/$SrTiO_3$ nanocomposite films were synthesized effectively via a cost-effective solution casting approach. The structural, thermal, morphological and electrical behavior of the synthesized PNC's was studied. The EMI shielding ability of the sample has also been tested in Ku-band (12–18 GHz) region. The presence of different

functional groups in the PNCs was affirmed using FTIR spectroscopic analysis. The XRD result affirms the cubic perovskite structure of the $SrTiO_3$ nanoparticles. The TGA thermogram unfolds the thermal stability of the PNCs. The morphological analysis shows the uniform distribution of the nanofiller within the polymer blend which enriches the interfacial interaction between the PNCs. The dielectric study reports that the PVC/PVDF/$SrTiO_3$ nanocomposite films show highest dielectric constant (ε 163 at 1 Hz, 150 °C) at 10 wt% of $SrTiO_3$ nanoparticles and low dielectric loss (Tan δ = 2.1, 1 Hz, 150 °C). From the EMI SE analysis, three main results have been inferred, (i) the SE of the PNCs intensify as the loading of $SrTiO_3$ nanoparticle increases, and this validates the potential of $SrTiO_3$ nanoparticles to block the EM noises. (ii) The prepared PNCs can operate as a dynamic EM absorber (73.9% absorption) as it has the proficiency to attenuate the impinging radiation through its high electric and magnetic dipoles at maximum filler content. (iii) The material acquires incredible great efficiency to blocks almost 99.68 to 99.69% of harmful EM noises (i.e., power of transmission around 0.31 to 0.32%). This negligible power of transmittance also ensures that the other 99.6% of destructive EM radiations have been attenuated through reflection and absorption mechanisms. Hence, the PVC/PVDF/$SrTiO_3$ nanocomposite films can make a powerful and efficient electromagnetic absorber in Ku-band.

Acknowledgements The author Jenifer Joseph is grateful to the VIT University management for facilitating FTIR, XRD and SEM analysis via VIT-DST-FIST scheme.

References

1. J. Mohammed, T.T.T. Carol, H.Y. Hafeez, D. Basandrai, G.R. Bhadu, S.K. Godara, S.B. Narang, A.K. Srivastava, Electromagnetic interference (EMI) shielding, microwave absorption and optical sensing properties of BaM/CCTO composites in Ku-band. Results Phys. **13**, 102307 (2019)
2. S. Bahel, K. Pubby, S.B. Narang, X-Band microwave reflection properties of samarium/bismuth-substituted barium lanthanum titanate ceramics. J. Electron. Mater. **46**(3), 1770–1776 (2017)
3. K. Pubby, S.B. Narang, S.K. Chawla, P. Kaur, Microwave absorption properties of cobalt-zirconium doped strontium hexaferrites in ku-frequency band. J. Supercond. Nov. Mag. **30**(12), 3465–3470 (2017)
4. M. Irfan, A. Shakoor, Structural, electrical and dielectric properties of dodecylbenzene sulphonic acid doped polypyrrole/nano-Y_2O_3 composites. J. Inorg. Organomet. Polym. Mater. **30**, 1287–1292 (2020)
5. T.T.T. Carol, J. Sharma, J. Mohammed, S. Kumar, A.K. Srivastava, Effect of temperature on the magnetic properties of nano-sized M-type barium hexagonal ferrites. AIPC **1860**(1), 020008 (2017)
6. N. Alonizan, L. Chouiref, K. Omri, M.A. Gondal, N. Madkhali, T. Ghrib, A.I. Alhassan, Photocatalytic activity, microstructures and luminescent study of Ti-ZS: M Nano-composites materials. J. Inorg. Organomet. Polym. Mater. **30**, 4372–4381 (2020)
7. P. Rani, M.B. Ahamed, K. Deshmukh, Structural, dielectric and EMI shielding properties of polyvinyl alcohol/chitosan blend nanocomposites integrated with graphite oxide and nickel oxide nanofillers. J. Mater. Sci. Mater. Electron. **32**, 764–779 (2021)
8. A.H. Kumar, M.B. Ahamed, K. Deshmukh, M.S. Sirajuddeen, Morphology, dielectric and emi shielding characteristics of graphene nanoplatelets, montmorillonite nanoclay and titanium dioxide nanoparticles reinforced polyvinylidenefluoride nanocomposites. J. Inorg. Organomet. Polym. Mater. (2021). https://doi.org/10.1007/s10904-020-01869-z
9. D. Basandrai, R.K. Bedi, A. Dhami, J. Sharma, S.B. Narang, K. Pubby, A.K. Srivastava, Radiation losses in the microwave X band in Al-Cr substituted Y-type hexaferrites. Chin. Phys. Lett. **34**(4), 044101 (2017)
10. X. Tang, K.A. Hu, Preparation and electromagnetic wave absorption properties of Fe-doped zinc oxide coated barium ferrite composites. Mater. Sci. Eng. B. **139**, 119–123 (2007)
11. J. Joseph, K. Deshmukh, K. Chidambaram, M. Faisal, E. Selvarajan, K.K. Sadasivuni, M.B. Ahamed, S.K.K. Pasha, Dielectric and electromagnetic interference shielding properties of germanium dioxide nanoparticle reinforced poly (vinyl chloride) and poly (methylmethacrylate) blend nanocomposites. J. Mater. Sci. Mater. Electron. **29**, 20172–20188 (2018)
12. T. Kaur, S. Kumar, S.B. Narang, A.K. Srivastava, Radiation losses in microwave Ku region by conducting pyrrole/barium titanate and barium hexaferrite based nanocomposites. J. Magn. Magn. Mater. **420**, 336–342 (2016)
13. K.K. Halder, M. Tomar, V.K. Sachdev, V. Gupta, Carbonized charcoal-loaded PVDF polymer composite: a promising EMI shielding material. Arab. J. Sci. Eng. **45**(1), 465–474 (2020)
14. N. Joseph, M.T. Sebastian, Electromagnetic interference shielding nature of PVDF-carbonyl iron composites. Mater. Lett. **90**, 64–67 (2013)
15. N. Yousefi, X. Sun, X. Lin, X. Shen, J. Jia, B. Zhang, B. Tang, M. Chan, J.K. Kim, Highly aligned graphene/polymer nanocomposites with excellent dielectric properties for high-performance electromagnetic interference shielding. Adv. Mater. **26**, 5480–5487 (2014)
16. S. Geetha, K.K. Satheesh Kumar, C.R. Rao, M. Vijayan, D.C. Trivedi, EMI shielding: methods and materials-a review. J. Appl. Polym. Sci. **112**, 2073–2086 (2009)
17. A.G. Koniuszewska, J.W. Kaczmar, Application of polymer based composite materials in transportation. Prog. Rubber Plast. Recycl. Technol. **32**(1), 1–24 (2016)
18. J. Joseph, K. Deshmukh, T. Tung, K. Chidambaram, S.K.K. Pasha, *3D Printing Technology of Polymer Composites and Hydrogels for Artificial Skin Tissue Implementations* (Springer, Cham, 2019).
19. A. Muzaffar, M.B. Ahamed, K. Deshmukh, S.K.K. Pasha, Dielectric properties and electromagnetic interference shielding studies of nickel oxide and tungsten oxide reinforced polyvinylchloride nanocomposites. Polym. Plast. Technol. Mater. **59**, 1667–1678 (2020)
20. P. Rani, M.B. Ahamed, K. Deshmukh, Dielectric and electromagnetic interference shielding properties of carbon black nanoparticles reinforced PVA/PEG blend nanocomposite films. Mater. Res. Exp. **7**, 064008 (2020)
21. Y.R. Kumar, K. Deshmukh, K.K. Sadasivuni, S.K.K. Pasha, Graphene quantum dot based materials for sensing, bio-imaging and energy storage applications: a review. RSC Adv. **10**, 23861–23898 (2020)
22. G.J. Thangamani, K. Deshmukh, N.A. Nambiraj, S.K.K. Pasha, Chemiresistive gas sensors based on vanadium pentoxide reinforced polyvinyl alcohol/polypyrrole blend nanocomposites for room temperature LPG sensing. Synth. Met. **273**, 116687 (2021)
23. P.L. Reddy, K. Deshmukh, T. Kovarik, N.A. Nambiraj, S.K.K. Pasha, Green chemistry mediated synthesis of cadmium sulphide/

polyvinyl alcohol nanocomposites: assessment of microstructural, thermal, and dielectric properties. Polym. Comp. **41**, 2054–2067 (2020)
24. K. Deshmukh, S.K.K. Pasha, Room temperature ammonia sensing based on graphene oxide integrated flexible polyvinylidenefluoride/cerium oxide nanocomposite films. Polym. Plast. Technol. Eng. **59**, 1429–1446 (2020)
25. B. Yuan, L. Yu, L. Sheng, K. An, X. Zhao, Comparison of electromagnetic interference shielding properties between single-wall carbon nanotube and graphene sheet/polyaniline composites. J. Phys. D **45**(23), 235108 (2012)
26. M. Arjmand, T. Apperley, M. Okoniewski, U. Sundararaj, Comparative study of electromagnetic interference shielding properties of injection molded versus compression molded multi-walled carbon nanotube/polystyrene composites. Carbon **50**, 5126–5134 (2012)
27. M. Hu, J. Gao, Y. Dong, K. Li, G. Shan, S. Yang, R.K.Y. Li, Flexible transparent PES/silver nanowires/PET sandwich-structured film for high-efficiency electromagnetic interference shielding. Langmuir **28**(18), 7101–7106 (2012)
28. M.F. Shakir, A.N. Khan, R. Khan, S. Javed, A. Tariq, M. Azeem, A. Riaz, A. Shafqat, H.M. Cheema, M.A. Akram, I. Ahmad, EMI shielding properties of polymer blends with inclusion of graphene nano platelets. Results Phys. **14**, 102365 (2019)
29. W. Kim, H. S. Song, B. O. Lee, K. Kwon, Y. Lim, M. Kim, Electrical properties of PVdF/PVP composite filled with carbon nanotubes prepared by floating catalyst method. Macromol. Res. **10**, 253–258 (2002)
30. V. Eswaraiah, V. Sankaranarayanan, S. Ramaprabhu, Functionalized graphene–PVDF foam composites for EMI shielding. Macromol. Mater. Eng. **296**, 894–898 (2011)
31. A. Muzaffar, M.B. Ahamed, K. Deshmukh, M. Faisal, Electromagnetic interference shielding properties of polyvinylchloride (PVC), barium titanate ($BaTiO_3$) and nickel oxide (NiO) based nanocomposites. Polym. Test. **77**, 105925 (2019)
32. N. Li, Y. Huang, F. Du, X. He, X. Lin, H. Gao, Y. Ma, F. Li, Y. Chen, P.C. Eklund, Electromagnetic interference (EMI) shielding of single-walled carbon nanotube epoxy composites. Nano. Lett. **6**(6), 1141–1145 (2006)
33. Y. Yang, M.C. Gupta, K.L. Dudley, Studies on electromagnetic interference shielding characteristics of metal nanoparticle-and carbon nanostructure-filled polymer composites in the Ku-band frequency. Micro Nano Lett. **2**, 85–89 (2007)
34. V. Eswaraiah, V. Sankaranarayanan, S. Ramaprabhu, Functionalized graphene–PVDF foam composites for EMI shielding. Macromol. Mater. Eng. **296**(10), 894–898 (2011)
35. K. Kim, S.J. Cho, S.T. Kim, I.J. Chin, H.J. Choi, Formation of two-dimensional array of multiwalled carbon nanotubes in polystyrene/poly (methyl methacrylate) thin film. Macromolecules **38**(26), 10623–10626 (2005)
36. S. Liu, S. Xiu, B. Shen, J. Zhai, L.B. Kong, Dielectric properties and energy storage densities of poly (vinylidenefluoride) nanocomposite with surface hydroxylated cube shaped $Ba_{0.6}Sr_{0.4}TiO_3$ nanoparticles. Polymers **8**(2), 45 (2016)
37. P. Rani, M.B. Ahamed, K. Deshmukh, Dielectric and electromagnetic interference shielding properties of Zeolite 13X and carbon black nanoparticles based PVDF nanocomposites. J. Appl. Polym. Sci. **138**, 50107 (2021)
38. H. Wang, D. Liu, X. Duan, P. Du, J. Guo, P. Liu, Facile preparation of high-strength polyaniline/polyvinyl chloride composite film as flexible free-standing electrode for supercapacitors. Mater. Des. **108**, 801–806 (2016)
39. S. Liu, S. Xue, S. Xiu, B. Shen, J. Zhai, Surface-modified Ba (Zr0.3Ti0.7) O_3 nanofibers by polyvinylpyrrolidone filler for poly (vinylidene fluoride) composites with enhanced dielectric constant and energy storage density. Sci. Rep. **6**, 26198 (2016)
40. M. Murugan, V.K. Kokate, A.A. Athawale, M.S. Bapat, M.H. Alhousami, Nanoparticles of barium and strontium titanates/epoxy resin as microwave absorbers. 10th International Conference on Electromagnetic Interference & Compatibility. (IEEE, 2008), pp. 457–462
41. N. Nuraje, K. Su, Perovskite ferroelectric nanomaterials. Nanoscale **5**(19), 8752–8780 (2013)
42. T. Xian, H. Yang, L. Di, J. Ma, H. Zhang, J. Dai, Photocatalytic reduction synthesis of $SrTiO_3$-graphene nanocomposites and their enhanced photocatalytic activity. Nanoscale Res. Lett. **9**(1), 1–9 (2014)
43. S.K. Mahto, S. Das, A. Ranjan, S.K. Singh, P. Roy, N. Misra, Chemical modification of poly (vinyl chloride) for blood and cellular biocompatibility. RSC Adv. **5**(56), 45231–45238 (2015)
44. S.M. Pawde, K. Deshmukh, Surface characterization of air plasma treated poly vinylidene fluoride and poly methyl methacrylate films. J. Appl. Polym. Sci. **49**, 808–818 (2009)
45. S. Shahabuddin, N. Muhamad Sarih, S. Mohamad, J. Joon Ching, $SrTiO_3$ nanocube-doped polyaniline nanocomposites with enhanced photocatalytic degradation of methylene blue under visible light. Polymers **8**(2), 27 (2016)
46 R. Arunkumar, R.S. Babu, M. Usha Rani, S. Kalainathan, Effect of PBMA on PVC-based polymer blend electrolytes. J. Appl. Polym. Sci. **134**(27), 44939 (2017)
47. M. Hasan, M. Lee, Enhancement of the thermo-mechanical properties and efficacy of mixing technique in the preparation of graphene/PVC nanocomposites compared to carbon nanotubes/PVC. Prog. Nat. Sci. Mater. **24**(6), 579–587 (2014)
48. L. Dong, X. Liu, Z. Xiong, D. Sheng, C. Lin, Y. Zhou, Y. Yang, Preparation of UV-blocking poly (vinylidene fluoride) films through SI-AGET ATRP using a colorless polydopamine initiator layer. Ind. Eng. Chem. Res. **57**(38), 12662–12669 (2018)
49. J. Liu, H. Shimanoe, S. Ko, H. Lee, C. Jo, J. Lee, S.H. Hong, H. Lee, Y.P. Jeon, K. Nakabayashi, J. Miyawaki, Highly chlorinated polyvinyl chloride as a novel precursor for fibrous carbon material. Polymers **12**(2), 328 (2020)
50. M.K. Mohanapriya, K. Deshmukh, K.K. Sadasivuni, G. Thangamani, K. Chidambaram, M.B. Ahamed, S.K.K. Pasha, Enhanced quality factor of polyvinyl formal (PVF) based nanocomposites filled with zinc oxide and carbon black nanoparticles for wireless sensing applications. Mater. Today Proc. **9**, 199–216 (2019)
51. K. Deshmukh, S.M. Khatake, G.M. Joshi, Surface properties of graphene oxide reinforced polyvinyl chloride nanocomposites. J. Polym. Res. **20**, 286 (2013)
52. K. Deshmukh, G.M. Joshi, Thermo-mechanical properties of poly (vinyl chloride)/graphene oxide as high performance nanocomposites. Polym. Test. **34**, 211–219 (2014)
53. G. Wang, Y. Deng, Y. Xiang, L. Guo, Fabrication of radial ZnO nanowire clusters and radial ZnO/PVDF composites with enhanced dielectric properties. Adv. Funct. Mater. **18**(17), 2584–2592 (2008)
54. J.L. Kaufman, S.H. Tan, K. Lau, A. Shah, R.G. Gambee, C. Gage, L. MacIntosh, A. Dato, P.N. Saeta, R.C. Haskell, T.C. Monson, Permittivity effects of particle agglomeration in ferroelectric ceramic-epoxy composites using finite element modeling. AIP Adv. **8**(12), 125020 (2018)
55. G. Wu, Y. Cheng, Y. Ren, Y. Wang, Z. Wang, H. Wu, Synthesis and characterization of γ-Fe_2O_3@ C nanorod-carbon sphere composite and its application as microwave absorbing material. J. Alloys Compd. **652**, 346–350 (2015)

56. G. Wu, Y. Cheng, Q. Xie, Z. Jia, F. Xiang, H. Wu, Facile synthesis of urchin-like ZnO hollow spheres with enhanced electromagnetic wave absorption properties. Mater. Lett. **144**, 157–160 (2015)
57. B. Dutta, E. Kar, G. Sen, N. Bose, S. Mukherjee, Lightweight, flexible NiO@ SiO_2/PVDF nanocomposite film for UV protection and EMI shielding application. Mater. Res. Bull. **124**, 110746 (2020)